COMMUNICATIONS PHYSICS

ARTICLE

https://doi.org/10.1038/s42005-019-0146-4 OPEN

The Mott to Kondo transition in diluted Kondo superlattices

Hovan Lee[1], Evgeny Plekhanov[1], David Blackbourn[1], Swagata Acharya[1] & Cedric Weber[1]

In condensed matter, a tremendous effort has been generated to realise Kondo lattices both experimentally and theoretically. The pursuit of independent magnetic moments, via charge localization, is paramount for applications in nanotechnology. Particularly, systems with simultaneous charge/spin degrees of freedom can manifest both Kondo spin quenching and Mott–Hubbard charge localization. Experimental frameworks illuminating pathways between the two are physically and technologically significant, and hardly observed in reality. Recent developments in controlling densities/temperatures of strongly correlated impurities on surfaces has opened up new possibilities. Such systems introduce mechanisms to study Kondo/Mott-physics interplay methodically. However, the pathway between Kondo physics and charge localization remains elusive. In this work, we investigate the phase diagram of superlattice structures of f-elements on substrates, assessing required conditions for obtaining Kondo superlattices. We unveil pathways between Kondo quenching and Mott localization, and identify non-trivial charge density waves emerging from the competition of charge localization and Kondo physics.

[1] King's College London, Theory and Simulation of Condensed Matter, The Strand, WC2R 2LS London, UK. Correspondence and requests for materials should be addressed to H.L. (email: hovan.lee@kcl.ac.uk)

Correlated adatoms expand upon the plethora of remarkable properties already existent in two-dimensional (2D) metallic surfaces. Stemming from the competition of localization and itinerant characters, such properties include: hybridization, superlattice self formation[1–6] and long range interactions[7–10]. Moreover, due to the comparatively low coordination between adatoms and substrate, single atom magnets in the form of Pt/Ho[11–13] have been debated and magnetic hysteresis of Er trimers on Cu have been observed[14]. These phenomena have attracted a wide academic interest, but also offer pathways towards industrial applications, for example as candidates for future atomic scale memory storage[15–17].

While the limits of Mott[18–20] superlattice and Kondo impurity behaviour are well documented, little is known about the transition between the densely packed (Mott) and the diluted (Kondo) limits of superlattice systems. Furthermore, although physical cases of 3d transition adatom[2,21–23] and rare-earth adatom[24–26] self-organization have been reported and justified with tight-binding models and kinetic Monte Carlo simulations[1,3,27–29], the quantum mechanism responsible for the formation of the superlattice, and the adatom-substrate requirements for self-formation are so far elusive.

To paint a picture of the phenomena observed in this work, an overview of impurity lattice physics is due: a single Kondo adatom within a material does not conserve momentum when scattering electrons. However, in this work, we discuss lattices whose unit cell contains Kondo impurities: Kondo lattices. Due to translational symmetries, Kondo scattering within such lattices conserve momentum, leading to coherent scattering and a decrease in resistivity below the Kondo temperature[30,31]. Interpreting requirements for constructing Kondo lattices will be essential in further understanding of correlated low-temperature research. Friedel oscillations[32] are another form of impurity-impurity communication. They describe electronic screening of an impurity and charge distribution on lattice sites. Different mechanisms have been proposed as the mediator for self-assembly. One such mechanism, which theorises how Friedel oscillations from two adatoms interact was proposed by Hyldgaard and Persson[33]. Lastly, Ruderman–Kittel–Kasuya–Yosida (RKKY) interactions[34–36] provide a mechanism for spin-spin coupling between f and/or d band electrons.

2D systems promote surface electron states. These states are formed with lower electron densities in comparison to the bulk electron states observed in three-dimensional systems. Therefore, electrons become localized under the effects of impurities, and the system becomes devoid of conduction band electrons. Since there is no scattering of conduction band electrons, this leads to an atomic limit behaviour at the lattice impurities. Moreover, substrate electrons are further localized by the impurity induced potential. Under these circumstances, a spin–spin interaction can occur between the impurities electrons and electrons localized near the impurities, forming singlet/triplet bound states. Lastly, due to the periodic structure of both the lattice and the impurity ionic potential, localization can occur around both the adatoms and on the substrate. Localization on substrate sites might be expected when inter-adatom distances become sufficiently large, and the conduction band of the substrate sufficiently high, permitting localization effects and realizing a charge density wave concomitant with a pseudogap formation. These effects have so far not been investigated, due to the complexity of the problem, which involves dealing with large unit-cells and the presence of strong correlations in the f-shell of the adatoms. Typically, such systems are beyond the reach of density functional theory, and even more so, from many body perturbative techniques like GW and its extensions.

In this work, we use a combination of dynamical mean field theory (DMFT) and tight binding calculations for a triangular lattice substrate, techniques which have been utilised on previous works concerning other superstructures[19,37,38]. We present our investigations into the generic properties of single orbital correlated adatom structure upon a triangular metallic substrate. This model is a canonical model for the description of a 4f1 orbital hybridized to a Ag(111) substrate. We systematically investigate the phase diagram as a function of correlation strength, substrate electronic density and adatom inter-distances, and outline the different phases obtained. We study the strength of correlations, quantified by the quasi-particle weight factor (Z), and examine the electron localization at the adatom and its impact on the correlated energy bands and Fermi surfaces.

We report a sharp Mott to Kondo transition as adatom spacing varies from a tightly packed solid to a diluted solid. We also report the stabilization of a charge density wave competing with Kondo physics at large inter-adatom distances. For any given superlattices, large mass renormalization are obtained at low and high-density regimes, corresponding to the limit of a weakly hybridized impurity, and the limit of a screened impurity respectively. These two phases are separated by the formation of a tightly bound triplet between the adatom and the substrate that exhibits a weak mass renormalization. In our view, the experimental realization of the Ce/Ag(111) superlattice falls in the latter regime, and our result shed light on the lack of evidence for Kondo physics as previously observed by spin-polarized scanning tunneling microscopy. Our work predicts that Kondo Lattices are obtained at intermediate adatom distances (5–9 substrate lattice sizes, L).

Results

Strength of correlations and emergent quasi-particles in the superlattice. First, we report the systematic study of the superlattice correlation strength, as function of the substrate electronic density and adatom distances, obtained by paramagnetic DMFT calculations (permitting fluctuating moments and correlations across adatoms, but not for long-range magnetic order). Correlation strength is measured by the adatom quasi-particle weight factor Z, obtained with the low energy imaginary component of Matsubara self-energy $\Sigma(i\omega_n)$, reported in Fig. 1a. The results outlined below correspond to Hubbard repulsion $U/t = 6$, where t is the tunnelling amplitudes across the substrate, typically $t = 0.75$ eV for the case of the Ag/Ce superlattice (we discuss results for this Coulomb repulsion thereafter, extended the calculations to other values of the Coulomb repulsion, see Supplementary Fig. 1).

We report a phase diagram in terms of the adatom electronic occupation n_f (all occupation refer to the single spin component only, as the calculations are paramagnetic). Although in our calculations we systematically change the chemical potential, we report the phase diagram in terms of the adatom occupancy. The total occupation is indeed a monotonic function of the adatom density at any finite temperature. We find two dominant regimes where correlation effects are large, at two nearly horizontal minima near the single spin adatom (f band) electron density $n_f = 0.3$ and 0.7, separated by a weakly correlated regime at half-filled adatom $n_f = 0.5$ across all values of U (see also Supplementary Figs. 1 and 2).

We report the electronic density of the substrate in Fig. 1b (blue denotes an empty substrate, and red the band insulating limit).

The energy resolved spectral weight $\rho(\omega)$, obtained respectively at adatom density $n_f = 0.7$ (see Fig. 1c), at half-filled adatom density $n_f = 0.5$ (see Fig. 1d, which also is concomitant with a

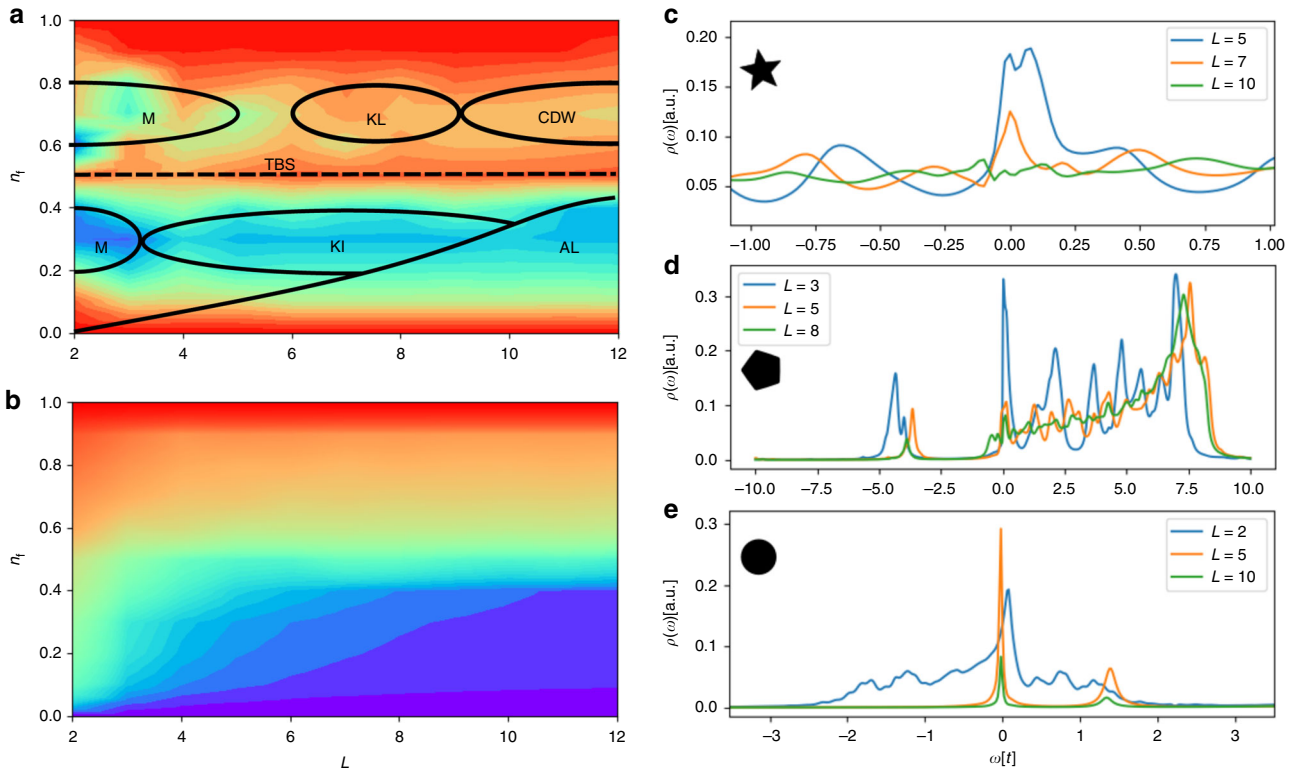

Fig. 1 Phase diagram. **a** Colour map of the quasi-particle weight Z for $U/t = 6$ and different lattice sizes L. Z is a measure of the strength of the electronic correlations induced by U, where the colour map indicates $Z = 0$ (blue) and $Z = 1$ (red). We identified three regions of interest in the phase diagram: for $n_f = 0.3$, $n_f = 0.5$ and $n_f = 0.7$. Each region is analyzed and split into phases (M - Mott, KI - Kondo impurity, AL - atomic limit, TBS - triplet bound state, KL - Kondo lattice and CDW - charge density wave). We report further in the text observables that characterize these phases. **b** Colour map of the substrate conduction band (CB) electronic density different substrate sizes L (blue for $n_{CB} = 0$ and red for $n_{CB} = 1$). The substrate's electronic states are empty in the lower right corner of the phase diagram, which indicates that in this region the adatom is decoupled from the substrate. **c**–**e** Total system density of states at $n_f = 0.7$, 0.5, 0.3 respectively. Each set of data is renormalized with the supercell size and shifted with respect to the chemical potential. This was done to allow for comparison between datasets

filling of two electron in total per unit-cell, meaning there is one electron in the substrate), and at low density $n_f = 0.3$ (see Fig. 1e).

In Fig. 2a, b, we report the spectral function $A(k, \omega)$ resolved in real frequencies ω and momentum k obtained for the same density. Note that, as the band structure is trivially folded due to the unit-cell construction of the periodic superlattice, we reconstruct the unfolded band structure of the original unit-cell of the substrate, which allows for comparison across different superlattices.

The Mott to Kondo crossover in the diluted solid. To investigate the correlated regions of the phase diagram (Fig. 1a), a polynomial regression was preformed on the adatom self-energy to obtain the electron scattering rate and the Kondo temperature (T_K) in the two correlated phases obtained at respectively $n_f = 0.3$ (Fig. 3a) and $n_f = 0.7$ (Fig. 3b). In both phases, we obtain a significant mass renormalization, concomitant with a large magnetic moment (see Supplementary Fig. 3), a required but not sufficient condition to obtain Kondo physics.

The Kondo temperature T_K, extracted from the low frequency hybridization (see Method section) was used here as a marker of the formation of a Kondo singlet. Note that T_K as extracted in this approximation provides the right trend, but is known to overestimate T_K. We obtain (see Fig. 3c, d) that a crossover occurs for both regions as the adatom distances reaches $L = 3$–4 for $n_f = 0.3$ and $L = 5$–6 for $n_f = 0.7$, respectively.

The calculation of the Kondo temperature has been validated by the measurement of the static local magnetic susceptibility χ

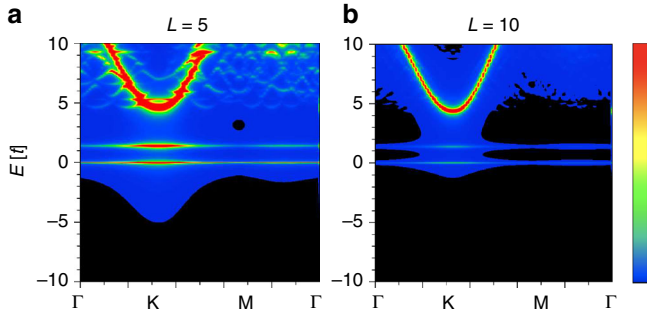

Fig. 2 Spectral weight. $A_{k,\omega}$, indicated with red (high) and blue/black (low) resolved in momentum and energy for $U/t = 6$ and $n_f = 0.3$ for **a** $L = 5$ and **b** $L = 10$. The adatom f state is strongly hybridized to the conduction band for intermediate lattice sizes ($L = 5$), but we observe a dehybridization of the adatom f state and conduction band at larger size $L = 10$. For the latter, the adatom is in the atomic limit (AL), as the conduction band remains weakly populated, as proposed in the discussion

($\omega = 0$) of the adatom, obtained from calculations carried out at different temperatures, this is presented in Fig. 4.

Weakly correlated triplet bound state. Finally, we investigated the region of the phase diagram that divides the two correlated regions obtained in the phase diagram (obtained at $n_f = 0.3$ and $n_f = 0.7$, respectively). At $n_f = 0.5$, which corresponds to the case

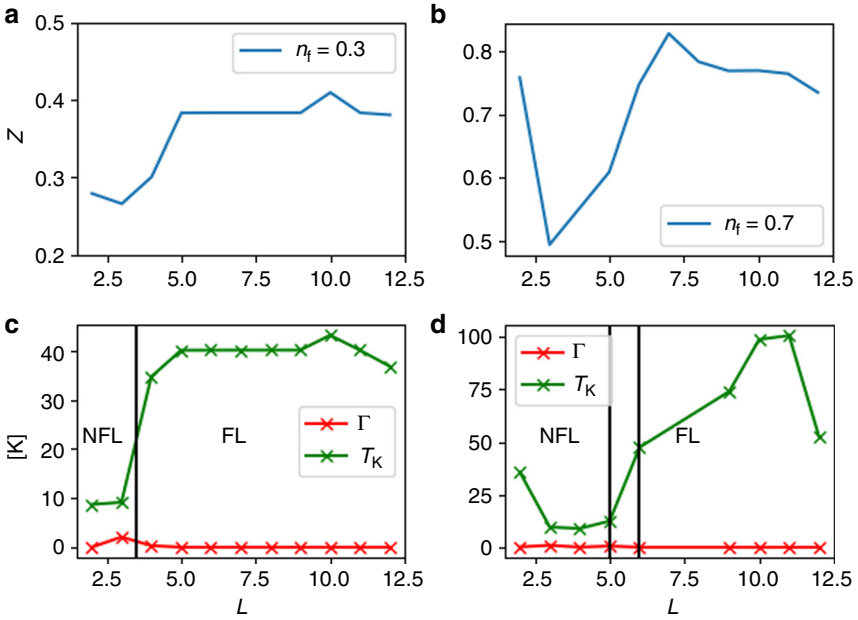

Fig. 3 Quasi-particle weight. Z across a range of lattice sizes L for $U/t = 6$ at adatom electron density **a** $n_f \sim 0.3$ and **b** $n_f \sim 0.7$. Scattering rate Γ and Kondo temperature T_K (as obtained by the formalism detailed in the Method section), both in units of Kelvin, in **c** $n_f \sim 0.3$ and **d** $n_f \sim 0.7$. At low density ($n_f \sim 0.3$), we observe a sharp first-order transition between non-Fermi liquid NFL and Fermi liquid FL for $L = 4$ (see the sharp onset of T_K at $L = 4$, concomitant with a reduction of the effective mass m^*). FL properties are eventually suppressed in the diluted limit ($L > 12$), as the atomic limit is obtained with the absence of electronic states in the substrate (see Discussion hereafter). For large density ($n_f \sim 0.7$) we observe a similar NFL/FL transition at $L = 6$

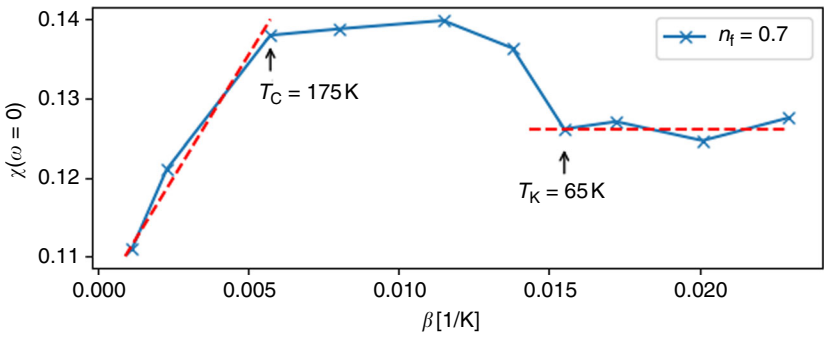

Fig. 4 Local magnetic susceptibility. $\chi(\omega = 0)$ of the adatom for $L = 6$ and $n_f = 0.7$, as a function of inverse temperature β. At high temperature ($T > T_C$), the susceptibility is proportional to $1/T$, indicating that the system is above the Curie temperature, whereas at low temperature ($T < T_K$), the susceptibility is temperature independent, showing that the system has entered into the Kondo regime

of a half-filled f level, we obtain the weakest mass renormalization and a regime of nearly free electrons (NFE) (see Fig. 1a). In Fig. 5, we report the integrated occupation over the supercell (both adatom and substrate). In particular, we find that the half-filled adatom f shell is obtained with a concomitant total charge of 2 electrons, and hence an occupation of a single electron per unit-cell on the substrate. The real space average charge (not shown) also reveals that the electron pair is localized in the unit cell around the adatom. This can be rationalized in a simple toy model, where 2 electrons are forming a bound state between the adatom and the three substrate neighbours (see Fig. 5). This toy model can be used as an approximation to capture the physics of the superlattice locally.

Mott localization driven by adatom interactions mediated by the substrate. We also extended our calculations to larger and smaller values of the correlation U. Whilst most results remain identical, we note that for the strong coupling regime ($U/t = 10$), the systems undergoes a charge localization for $L = 9$ for $n_f = 0.7$, followed by the formation of a pseudogap and the suppression of the Kondo resonance (see Supplementary Fig. 4). The localization is directly observed in the real space electronic density (compare Fig. 6a, b with Fig. 6c). Albeit observed in all calculations that electrons localized naturally around the adatoms, due to the attractive ionic potential, the localization induced by the Coulomb repulsion in this particular regime of parameters happens in-between the adatoms.

Discussion

In Fig. 1a, low n_f, we obtain here that the quasi-particle state is localized at the adatom. As n_f increases, however, Z also increases, reaching a maximum when the adatom is exactly half-filled. Although we might naively expect that the reduction of the mass renormalization is associated with a delocalization of the charge, we observe that the electron remain tightly bound to the adatom location. In our view, this is associated with the creation of a two-electron tightly bound triplet state between the adatom and the substrate (see Fig. 5). Finally, at densities larger than two-electron per unit-cell, we obtain another localization process near $n_f = 0.7$ with a concomitant increase of the mass renormalization.

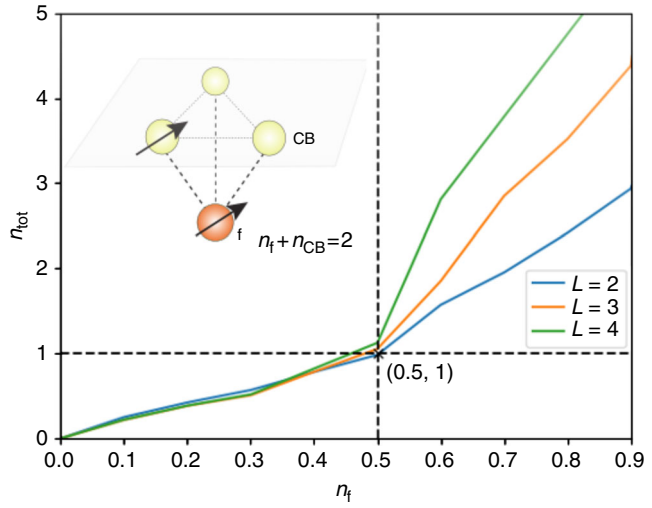

Fig. 5 Adatom electron occupation. Number of electrons within the supercell N_{tot} as a function of n_f for $U = 6$. Across all lattice size L, the graph follows the same linear increase from an empty system to ($n_f = 0.5$, $N_{tot} = 1$). We conclude that (taking both spins into account) when the adatom is singly occupied, the conduction band must also be singly occupied, allowing singlet/ triplet states between the adatom and substrate to form

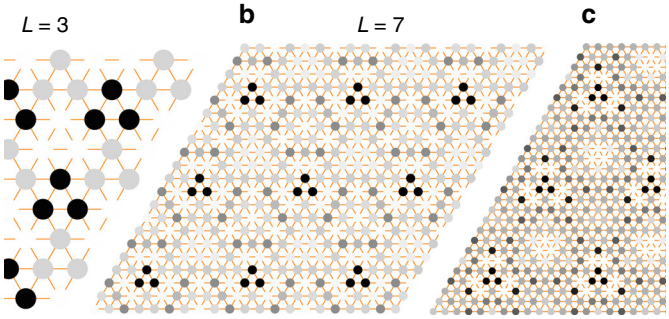

Fig. 6 Charge density wave. Real space electronic density n_{CB} of the substrate conduction band for the strongly coupled regime and $n_f \sim 0.7$ for **a** $L = 3$, **b** $L = 7$ and **c** $L = 9$. Black (white) colours indicate large (small) electronic density. For $L = 3$, we observe localized states around the adatom (the adatom, not shown, is located at the centre of the black circles). As L increases, we observe a delocalization, which is concomitant with Kondo physics (see Discussion hereafter). For the limit of diluted solids, corresponding to $L = 9$ and larger, we observe the formation of a charge density wave (CDW), where localized states develop in between adatoms. The CDW is concomitant with the formation of a pseudogap (see Discussion hereafter)

Moving onto Fig. 1b. As expected, at low occupation of the adatom, the substrate is empty, and we obtain the limit of an impurity in vacuum (atomic limit, AL). This limit is not physical and provides a lower bound on the adatom occupation for a given superlattice structure. Additionally, at small adatom distances L, we observe a rapid filling of the substrate upon increasing the adatom occupation, an effect related to the Coulomb repulsion U at the adatom site, that prevents an occupation of more than one electron and induces a charge transfer to the substrate.

At high electron density $n_f = 0.7$ (see Fig. 1c), we observe the emergence of a resonance, that starts to develop at $L = 5$, and becomes resonant at $L = 7$, and ultimately vanishes at $L = 10$. We associate this feature to the presence of a screened Kondo singlet (see discussion thereafter). We note that at the same density, we observe at large adatom distances $L > 9$ the formation of a charge density wave, where electron on the substrate localize half-way in-between adatoms, with the opening of a pseudogap in the spectral density (see Supplementary Figs. 1 and 4). This phase is denoted as CDW in the phase diagram.

The spectral feature of the weakly correlated region at $n_f = 0.5$ (see Fig. 1d) exhibits a large degree of hybridization between the adatom and substrate. We associate this state to a Triplet Bound State (TBS) formation.

The low density regime exhibits (see Fig. 1e) sharp features that corresponds to the localized states at the adatom. We obtain a transition from a broad feature, reminiscent the correlated metal, to a narrow spectral feature at the Fermi level obtained at adatom distances $L > 4$. This is fingerprint of a localized electron at the adatom location, which we denote at a Kondo impurity (KI). Ultimately, the KI localized quasi-particle states converges to the atomic limit (AL) at large adatom separation.

In Fig. 2, we observe that the adatom are strongly hybridized to the substrate for $n_f = 0.3$, $L = 5$ (Fig. 2a), as shown by the fluctuations induced in the substrate bands by the adatom, but dehybridize at larger adatom distance $L = 10$ (Fig. 2b), a fingerprint that the atomic limit has been reached (AL).

Regarding Fig. 3c, for the limit of the Kondo impurity ($n_f = 0.3$), the system enters into the Kondo regime abruptly via an abrupt transition (see Supplementary Fig. 2) between a non Fermi liquid at short adatom distances to a Fermi liquid at intermediate adatom distances (a linear behaviour of the self-energy as a function of the Matsubara frequency is obtained in the self-energy, a signature of a Fermi liquid, see Supplementary Fig. 2).

For $n_f = 0.7$ (Fig. 3d), the crossover is continuous and, unlike the abrupt change obtained between the NFL to FL regime obtained at $n_f = 0.3$, an increase in the mass renormalization occurs simultaneously with the large increase of T_K at $n_f = 0.7$.

In Fig. 4, we observe that the system manifests true Kondo behaviour in the large density regime $n_f = 0.7$, for temperatures lower than $T = 0.007 \times t$, which corresponds to $\approx 60°$ K (the tunneling amplitude for the silver substrate is $t = 0.75$ eV). We, therefore, identify the region of the phase diagram $L > 5$ and $n_f = 0.7$ as a Kondo lattice (KL): a lattice of independent screened magnetic moments. At large temperature $T > 0.02 \times t$, we recover the usual Curie Weiss law, which describes a fluctuation moment.

Moreover, in the low density limit ($n_f = 0.3$), we find that the local susceptibility remains small at all temperatures with weak temperature dependence ($\chi \sim 0.02$), as expected for a system which exhibits a large degree of localization due to correlation effects. We also note that a larger Coulomb repulsion $U/t = 10$ opens a gap and suppresses the resonance obtained in this regime (see Supplementary Fig. 4), gaping in turn the fluctuations associated with the magnetic moment by Mott physics. Due to the low occupation of the conduction band, we consider the region $L > 3$ and $n_f = 0.3$ as a system of Kondo impurities (KI).

The solution of the 2 electron model in Fig. 5 gives a bound triplet ground state for any realistic values of the screened Coulomb interaction U ($U < 11$ eV). For $U > 11$ eV, we obtain a singlet ground state. It is worth noting that this limit was obtained by renormalizing the hopping parameters between the substrate atoms to recover the bandwidth of the conduction band, as those have been integrated out in this simple picture (without this renormalization, the U separating the singlet from the triplet is larger). We, therefore, conclude that for this region of the phase diagram, we obtain triplet bound electron pairs localized around the adatoms. Note that the triplet can be seen as an uncorrelated state, as the Pauli principle excludes the double occupations. In our view, this phenomena explains the nearly free electron regime, separating the correlated phases at low and high n_f.

Lastly, regarding the Coulombic localization effects in Fig. 6. In our view, this effect is driven by the two-body potential induced

by the interference energies between Friedel oscillations. This two-body adatom interaction, mediated by surface state electrons, is an oscillating function of the adatom distance (similarly to the RKKY interaction), and is parametrized by the electronic mass. In the free electron model, its oscillations are involving distances larger than 11 lattice spacings, and therefore does not play a role in our calculations for $L < 11$. Furthermore, this interaction is also suppressed when the states at the Fermi level are absent (as it is the case in the low density regime $n_f = 0.3$ at large $U/t = 10$ that opens a gap).

However, at large density $n_f = 0.7$, the adatom mediated interaction is modified by the large mass renormalization induced by the local Hubbard U term, and produces an attractive potential in-between the adatoms.

We emphasize that this CDW is fundamentally different from Friedel oscillations (FO), where the amplitude decreases as distance from impurity increases. Secondly, as discovered by Chatterjee et al.[39]. the amplitude of FO decreases as U increases, in contradiction to our observation in the Kondo superlattice. Furthermore, the charge localization, in our measurements, is obtained in the large U limit ($U/t = 10$), and is concomitant with a renormalization of the electronic mass (see Supplementary Fig. 1). We associate hence the CDW to a charge ordering induced by the narrowing of the conduction band induced by correlation. The electronic localization is associated with the opening of a pseudogap.

Methods

In this paper, we have used the following computational setup in order to model the deposition of Ce adatoms on Ag substrate: the Ag substrate was modelled by a 2D triangular lattice of Ag 5s orbitals, while the Ce adatom 4f orbital was represented by an additional site connected with its three nearest neighbour Ag atoms. The heavy deposited Ce adatom hybridize with the substrate, and also induce an attractive ionic potential on the three neighbours of the substrate.

In this work, we use the dynamical mean-field theory (DMFT) approximation. Heavy f-materials have been extensively studied by DMFT, which captures well both the itinerant and localized behaviour of the electrons in f-materials[40–44]. In the DMFT formalism, the adatom (Ce) sites with the on-site U are treated as strongly correlated orbitals, while the conduction band of the substrate (Ag sites) are considered as uncorrelated. More formally, the Hamiltonian of the system considered here reads in real-space as:

$$H = -t\sum_{\langle i,j\rangle,\sigma} c^{\dagger}_{i\sigma}c_{j\sigma} + \sum_{\sigma,k}\varepsilon_{imp}f^{\dagger}_{\sigma,k}f_{\sigma,k} + \sum_{i,\sigma} V_i c^{\dagger}_{i\sigma}c_{i\sigma} + \sum_{\langle i,k\rangle,\sigma}\left(V_{if}c^{\dagger}_{i\sigma}f_{\sigma,k} + \text{h.c.}\right) + U\sum_{\sigma,k} n_{f\uparrow,k}n_{f\downarrow,k} + \mu N_{tot}, \quad (1)$$

where t is the inter-substrate hopping (in our calculation t is the energy scale, for the case of a Ag(111) substrate, $t = 0.75$ eV), ε_{imp} is the adatom energy level, U the adatom Hubbard repulsion, μ the chemical potential and h.c. denotes Hermitian conjugate. $c^{(\dagger)}_{i\sigma}$ and $f^{(\dagger)}_{i\sigma}$ are the Fermionic annihilation (creation) operators of the site i, spin σ, surface state and the adatom respectively. V_i describes the on-site potential asserted upon the substrate by the adatom (as described in ref. [1]). And lastly, the adatom/substrate hopping parameter $V_{if} = V^{*}_{fi} = t_{Ad}$ is assumed finite for three of the substrate sites, otherwise it is zero. This assumption can be justified through consideration of the triangular substrate[1,4]. The schematic view of our computational setup is shown in Fig. 7.

In analogy with DFT+DMFT, the calculation requires convergence with respect to the number of k-points in the Brillouin zone of substrate lattice. Calculations carried out in this work were computationally intensive, convergence in some cases required 100×100 sixfold reduced k-points (triangular substrate symmetry). Without any simplifications, calculations of each k-point scales as $n_{freq}N^3$, for number of sites N and number of Green's function frequency points $n_{freq} = \mathcal{O}(1000)$. For the largest lattice size considered, $L = 15$, of the order of $1000^{*}225^3$ calculations was needed to invert the Hamiltonian to calculate the Green's function for a single DMFT iteration.

In DMFT, we have employed an exact diagonalization (ED) solver improved by using the cluster perturbation theory (CPT). The ED solver[45–47] uses a finite discretization approximation of hybridization $\Delta(i\omega_n)$ function, which induces finite discretization errors[48]. As the size of the basis used to represent the Hamiltonian scales exponentially with the number of bath energies in the system, solving the eigenvalue problem is not computationally achievable if the number of bath orbitals is typically larger than 15. ED-CPT[49] bypasses this problem by utilizing a small number of bath systems and incorporating additional bath sites in order to mimic the effect of coupling to an infinite bath, which was used in our work to check that no remaining systematic error due to the bath discretization was obtained in our calculations. Finally, we have used Lichtenstein's double counting scheme[50].

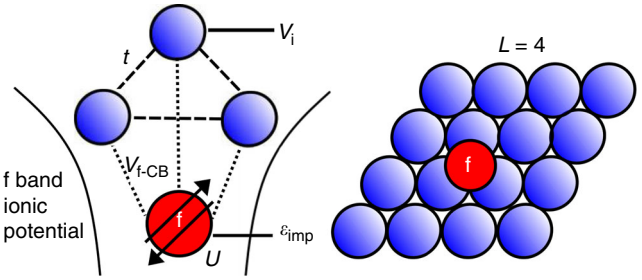

Fig. 7 Cartoon picture of the dynamical mean field theory setup. The model includes the conduction band of the substrate (depicted by the blue circles) and the concomitant Hamiltonian parameters. The correlated adatom (red circle) sits in between three sites of the substrate (blue circles)

Sherman-Morrison. Calculation of the full lattice Green's function $G(k)$ involves a matrix inversion at each k-point and ω. In the case of large supercell sizes this becomes a bottleneck of the formalism. An optimization is possible here due to the fact that the matrix to be inverted contains a large number of empty entries. This is due to the properties of the supercell: the self-energy is non-zero only at the adatom, and the hybridization between the adatom and the substrate occurs only on three sites of the substrate. Therefore, to reduce the computational load, the Sherman-Morrison algorithm[51] was implemented to update the full Green's function $G(k)$ from the substrate Green's function $G_0(k)$:

$$G_0^{-1}(k) = \begin{bmatrix} i\omega - V_i & -t & -t & 0 & \dots \\ -t & i\omega - V_i & -t & -t & \dots \\ -t & -t & i\omega - V_i & -t & \dots \\ 0 & -t & -t & i\omega & \dots \\ \vdots & \vdots & \vdots & \vdots & \ddots \end{bmatrix}, \quad (2)$$

$$G^{-1}(k) = \left[\begin{array}{cccc|c} & & & & V_{if} \\ & & G_0^{-1}(k) & & V_{if} \\ & & & & V_{if} \\ & & & & 0 \\ & & & & \vdots \\ \hline V_{if} & V_{if} & V_{if} & 0\ \dots & \epsilon_f - \Sigma \end{array}\right]. \quad (3)$$

Here V_{if}, ε_f, t, and V_i are defined in (1), $i\omega_n$ is the n's Matsubara frequency, while the substrate sites are ordered in such a way that the three sites connected to the adatom are listed first.

G_0 is obtained via matrix products for all n_{freq} (N^2 operations), G is then updated from G_0. Since only three substrate sites hybridizes with the adatom, the updating process scales linearly with N.

Kondo physics. In order to extract the Kondo physics fingerprints from our DMFT results, we have calculated the scattering rate Γ and Kondo temperature T_K.

In order to estimate Γ, we performed the polynomial regression with the following low frequency, low-temperature expansion of $\Sigma''(i\omega_n)$ in the Kondo regime[52]:

$$\Sigma''(i\omega_n) = a + \left(1 - \frac{1}{Z}\right)\omega_n - \frac{1}{2Z^2\Delta''(i\omega_n)}\omega_n^2. \quad (4)$$

Γ is obtained from the above parameters a and Z as follows:

$$\Gamma = -\frac{a}{Z}. \quad (5)$$

We used[53] the following definition of the Kondo temperature T_K after Hewson's renormalized perturbation theory[54] of the Anderson impurity model (AIM):

$$T_K = -\frac{\pi Z}{4}\Delta''(i\omega_n)|_{\omega_n \to 0} \quad (6)$$

where Δ'' is the imaginary part of the resonant level scattering width as defined in ref. [54].

Triplet bound state toy model. Here we briefly outline the simple toy model used to analyze the regime of the phase diagram, where we have two electrons per unit-

cell. As we observed in the superlattice calculations that the electronic states are localized around the adatoms, we solve the isolated plaquette of three substrate atoms connected to the adatom site. This Hamiltonian includes a local Coulomb repulsion U on the adatom site, an hybridization between the adatom and the three substrate atoms, and hopping across the substrate atoms. The impurity energy and hybridization are the same as the one treated in the full DMFT calculations, whereas the hopping across the substrate elements is renormalized to account for the bandwidth of the full calculation. Upon diagonalizing this Hamiltonian and finding the ground state, we then evaluate the expectation value of the spin correlator K operator between the adatom and one of the substrate atom, which identifies a singlet (triplet) ground state if $K < 0$ ($K > 0$). We identify the first-order transition between the triplet state at small U and the singlet state at large U (see Supplementary Fig. 5). Interestingly, we find that the critical U to obtain a singlet state is larger than all realistic U considered in our calculation. This suggests that in the limit of low occupation, pairs of electrons will form a triplet state for realistic values of the Coulomb repulsion.

This triplet state is indeed a multiplet that also includes the polarized contribution with two electrons of same spin, and exhibit a lower degree of correlation. Indeed, in the $S^z_{\mathrm{tot}} = \pm 1$ sectors, there are no contributions from the Coulomb energy, as observed in the phase diagram near the $n_f = 0.5$ region, where the mass renormalization is weak. We attribute hence this region of the phase diagram to a triplet bound state.

Data availability

Selected input and output files that support the findings of this study have been deposited in figshare with the identifier: https://doi.org/10.6084/m9.figshare.7796636.

Code availability

A.zip file of the code that support the findings of this study has been deposited in figshare with the identifier: https://doi.org/10.6084/m9.figshare.7796627.

Received: 26 October 2018 Accepted: 20 March 2019
Published online: 13 May 2019

References

1. Ternes, M. et al. Scanning-tunneling spectroscopy of surface-state electrons scattered by a slightly disordered two-dimensional dilute "solid": Ce on ag (111). *Phys. Rev. Lett.* **93**, 146805 (2004).
2. Zhang, X. P. et al. Atomic superlattice formation mechanism revealed by scanning tunneling microscopy and kinetic monte carlo simulations. *Phys. Rev. B* **81**, 125438 (2010).
3. Cao, R. et al. Self-organized Gd atomic superlattice on Ag(111): Scanning tunneling microscopy and kinetic Monte Carlo simulations. *Surf. Sci.* **610**, 65–69 (2013).
4. Blackbourn D. *An Investigation Into Self Assembled Super-lattices of Strongly Correlated Adatoms on Metallic Surfaces Through The Use of Dynamical Mean Field Theory*, Ph.D. thesis, King's College London (2016).
5. Smilgies, D.-M. & Hanrath, T. Superlattice self-assembly: watching nanocrystals in action. *Europhys. Lett.* **119**, 28003 (2017).
6. Waltmann, T., Waltmann, C., Horst, N. & Travesset, A. Many body effects and icosahedral order in superlattice self-assembly. *J. Am. Chem. Soc.* **140**, 8236–8245 (2018).
7. Nanayakkara, S. U., Sykes, E. C. H., Fernández-Torres, L. C., Blake, M. M. & Weiss, P. S. Long-range electronic interactions at a high temperature: Bromine adatom islands on cu(111). *Phys. Rev. Lett.* **98**, 206108 (2007).
8. Shytov, A. V., Abanin, D. A. & Levitov, L. S. Long-range interaction between adatoms in graphene. *Phys. Rev. Lett.* **103**, 016806 (2009).
9. Morgenstern, K. & Rieder, K.-H. Long-range interaction of copper adatoms and copper dimers on ag(1 1 1). *New J. Phys.* **7**, 139 (2005).
10. Wahlström, E., Ekvall, I., Olin, H. & Walldén, L. Long-range interaction between adatoms at the cu(111) surface imaged by scanning tunnelling microscopy. *Applied Physics A* **66**, 1107–1110 (1998).
11. Miyamachi, T. et al. Stabilizing the magnetic moment of single holmium atoms by symmetry. *Nature* **503**, 242 (2013).
12. Donati, F. et al. Magnetism of ho and er atoms on close-packed metal surfaces. *Phys. Rev. Lett.* **113**, 237201 (2014).
13. Shick, A. B., Shapiro, D. S., Kolorenc, J. & Lichtenstein, A. I. Magnetic character of holmium atom adsorbed on platinum surface. *Sci. Rep.* **7**, 2751 (2017).
14. Singha, A. et al. Magnetic hysteresis in er trimers on cu(111). *Nano. Lett.* **16**, 3475–3481 (2016).
15. Loth, S., Baumann, S., Lutz, C. P., Eigler, D. M. & Heinrich, A. J. Bistability in atomic-scale antiferromagnets. *Science* **335**, 196–199 (2012).
16. Khajetoorians, A. A. & Heinrich, A. J. Toward single-atom memory. *Science* **352**, 296–297 (2016).
17. Natterer, F. D. et al. Reading and writing single-atom magnets. *Nature* **543**, 226 (2017).
18. Ming, F. et al. Realization of a hole-doped mott insulator on a triangular silicon lattice. *Phys. Rev. Lett.* **119**, 266802 (2017).
19. Yi, S., Lee, H., Choi, J.-H. & Cho, J.-H. Nature of the insulating ground state of the two-dimensional sn atom lattice on sic(0001). *Sci. Rep.* **6**, 30598 (2016).
20. Dou, X., Kotov, V. N. & Uchoa, B. Designing quantum spin-orbital liquids in artificial mott insulators. *Sci. Rep.* **6**, 31737 (2016).
21. Repp, J. et al. Substrate mediated long-range oscillatory interaction between adatoms: Cu/cu (111). *Phys. Rev. Lett.* **85**, 2981–2984 (2000).
22. Knorr, N. et al. Long-range adsorbate interactions mediated by a two-dimensional electron gas. *Phys. Rev. B* **65**, 115420 (2002).
23. Negulyaev, N. N. et al. Effect of strain relaxations on heteroepitaxial metal-on-metal island nucleation and superlattice formation: Fe on cu(111). *Phys. Rev. B* **79**, 195411 (2009).
24. Silly, F. et al. Creation of an atomic superlattice by immersing metallic adatoms in a two-dimensional electron sea. *Phys. Rev. Lett.* **92**, 016101 (2004).
25. Negulyaev, N. N. et al. Melting of two-dimensional adatom superlattices stabilized by long-range electronic interactions. *Phys. Rev. Lett.* **102**, 246102 (2009).
26. Singha, A. et al. Magnetic hysteresis in er trimers on cu(111). *Nano. Lett.* **16**, 3475–3481 (2016).
27. Negulyaev, N. N. et al. Self-organization of ce adatoms on Ag(111): A kinetic monte carlo study. *Phys. Rev. B* **74**, 035421 (2006).
28. Schiffrin, A. et al. Self-aligning atomic strings in surface-supported biomolecular gratings. *Phys. Rev. B* **78**, 035424 (2008).
29. Hu, J., Teng, B., Wu, F. & Fang, Y. Fe nanostructures stabilized by long-range interactions on cu(111): kinetic monte carlo simulations. *New J. Phys.* **10**, 023033 (2008).
30. Generalov, A. et al. Insight into the temperature dependent properties of the ferromagnetic Kondo lattice YbNiSn. *Phys. Rev. B***95**, 184433 (2017).
31. Minami, S. & Kawamura, H. Low-temperature magnetic properties of the Kondo lattice model in one dimension. *J. Phys. Soc. Jpn.* **84**, 044702 (2015).
32. Friedel, J. XIV. The distribution of electrons round impurities in monovalent metals. *Philos. Mag.***43**, 153–189 (1952).
33. Hyldgaard, P. & Persson, M. Long-ranged adsorbate-adsorbate interactions mediated by a surface-state band. *J. Phys. Condens. Matter.* **12**, L13 (2000).
34. Ruderman, M. A. & Kittel, C. Indirect exchange coupling of nuclear magnetic moments by conduction electrons. *Phys. Rev.* **96**, 99–102 (1954).
35. Kasuya, T. A theory of metallic ferro- and antiferromagnetism on zener's model. *Prog. Theo.Phys.* **16**, 45–57 (1956).
36. Yosida, K. Magnetic properties of cu-mn alloys. *Phys. Rev.* **106**, 893–898 (1957).
37. Hansmann, P., Ayral, T., Vaugier, L., Werner, P. & Biermann, S. Long-range coulomb interactions in surface systems: A first-principles description within self-consistently combined *gw* and dynamical mean-field theory. *Phys. Rev. Lett.* **110**, 166401 (2013).
38. Hwang, J. et al. Emergence of kondo resonance in graphene intercalated with cerium. *Nano. Lett.* **18**, 3661–3666 (2018).
39. B. Chatterjee, J. Skolimowski, K. Makuch, K. & Byczuk. Real-space dynamical mean-field theory of Friedel oscillations in strongly correlated electron systems, ArXiv e-prints arXiv:1807.08566.
40. Pourovskii, L. V., Amadon, B., Biermann, S. & Georges, A. Self-consistency over the charge density in dynamical mean-field theory: A linear muffin-tin implementation and some physical implications. *Phys. Rev. B* **76**, 235101 (2007).
41. Amadon, B. et al. Plane-wave based electronic structure calculations for correlated materials using dynamical mean-field theory and projected local orbitals. *Phys. Rev. B* **77**, 205112 (2008).
42. Lichtenstein, A. I. *Electronic Structure of Complex Oxides* 167 (Springer, Netherlands, 2013).
43. Lechermann, F. et al. Dynamical mean-field theory using wannier functions: A flexible route to electronic structure calculations of strongly correlated materials. *Phys. Rev. B* **74**, 125120 (2006).
44. Plekhanov, E. et al. Many-body renormalization of forces in *f*-electron materials. *Phys. Rev. B* **98**, 075129 (2018).
45. Caffarel, M. & Krauth, W. Exact diagonalization approach to correlated fermions in infinite dimensions: Mott transition and superconductivity. *Phys. Rev. Lett.* **72**, 1545–1548 (1994).
46. Capone, M. L. de' Medici, A. Georges, Solving the dynamical mean-field theory at very low temperatures using the lanczos exact diagonalization. *Phys. Rev. B* **76**, 245116 (2007).
47. Liebsch, A. & Ishida, H. Temperature and bath size in exact diagonalization dynamical mean field theory. *J. Phys. Condens. Matter.* **24**, 053201 (2012).
48. Lanczos, C. An iterative method for the solution of the eigenvalue problem of linear differential and integral operators. *J. Res. Natl. Bur. Stand. B* **45**, 255–282 (1950).

49. Weber, C., Amaricci, A., Capone, M. & Littlewood, P. B. Augmented hybrid exact-diagonalization solver for dynamical mean field theory. *Phys. Rev. B***86**, 115136 (2012).
50. Pavarini, E., Koch, E., Lichtenstein, A. & Vollhardt, D (eds). *DMFT at 25: Infinite Dimensions* Ch. 8 (Forschungszentrum Jülich Zentralbibliothek, Verlag, Jülich, 2014)
51. Sherman, J. & Morrison, W. J. Adjustment of an inverse matrix corresponding to a change in one element of a given matrix. *Ann. Math. Statist.* **21**, 124–127 (1950).
52. Costi, T. A., Hewson, A. C. & Zlatic, V. Transport coefficients of the Anderson model via the numerical renormalization group. *J. Phys. Condens. Matter.* **6**, 2519–2558 (1994).
53. Surer, B. et al. Multi-orbital Kondo physics of Co in Cu hosts. *Phys. Rev. B* **85**, 085114 (2012).
54. Hewson, A. C. The strong coupling fixed-point revisited. *J. Physical. Soc. Japan* **74**, 8–15 (2005).

Acknowledgements

This research was supported by EPSRC (EP/M011038/1 and also EP/R02992X/1) and the Simons Many-Electron Collaboration. C.W. gratefully acknowledges the support of NVIDIA Corporation, ARCHER UK National Supercomputing Service. We are grateful to the UK Materials and Molecular Modelling Hub for computational resources, which is partially funded by EPSRC (EP/P020194/1).

Author contributions

H.L. and D.B. carried out the simulations in this project, analysed the data and wrote this article. C.W. supervised the project. S.A., E.P. and C.W. contributed to the writing this article.

Additional information

Supplementary information accompanies this paper at https://doi.org/10.1038/s42005-019-0146-4.

Competing interests: The authors declare no competing interests.

Reprints and permission information is available online at http://npg.nature.com/reprintsandpermissions/

Publisher's note: Springer Nature remains neutral with regard to jurisdictional claims in published maps and institutional affiliations.